Provided for non-commercial research and education use.
Not for reproduction, distribution or commercial use.

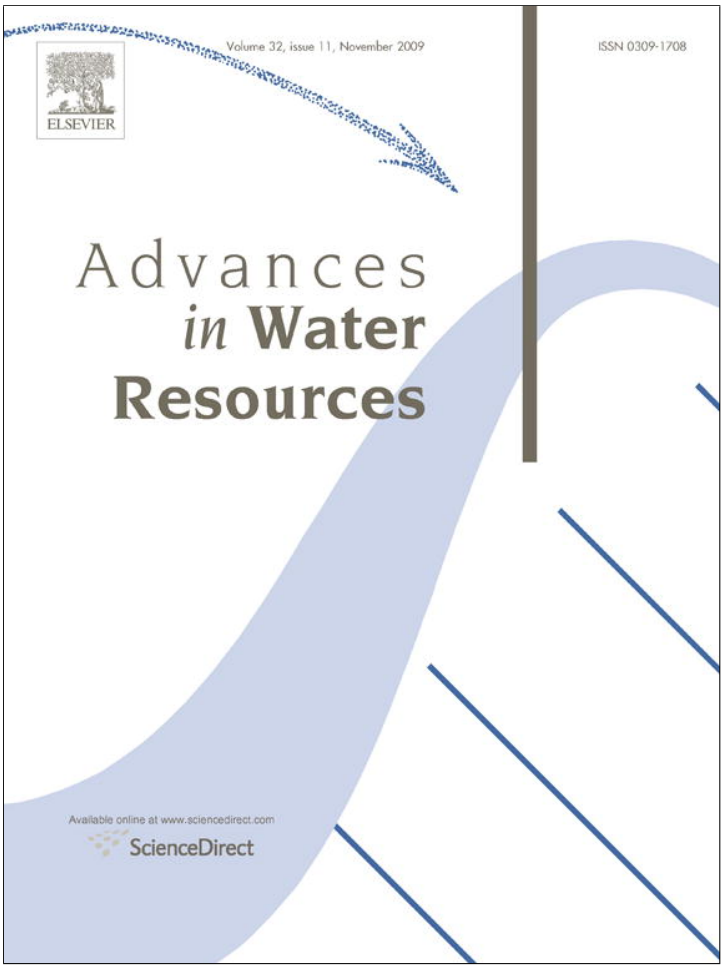


This article appeared in a journal published by Elsevier. The attached copy is furnished to the author for internal non-commercial research and education use, including for instruction at the authors institution and sharing with colleagues.

Other uses, including reproduction and distribution, or selling or licensing copies, or posting to personal, institutional or third party websites are prohibited.

In most cases authors are permitted to post their version of the article (e.g. in Word or Tex form) to their personal website or institutional repository. Authors requiring further information regarding Elsevier's archiving and manuscript policies are encouraged to visit:

http://www.elsevier.com/copyright

Author's personal copy

Advances in Water Resources 32 (2009) 1632–1640

Contents lists available at ScienceDirect

Advances in Water Resources

journal homepage: www.elsevier.com/locate/advwatres

# Lattice-Boltzmann simulations of the capillary pressure–saturation–interfacial area relationship for porous media

Mark L. Porter [a,*], Marcel G. Schaap [b], Dorthe Wildenschild [a]

[a] School of Chemical, Biological and Environmental Engineering, Oregon State University, 102 Gleeson Hall, Corvallis, OR 97331, USA
[b] Department of Soil, Water and Environmental Sciences, University of Arizona, Tucson, AZ 85721, USA

ARTICLE INFO

*Article history:*
Received 17 June 2009
Received in revised form 21 August 2009
Accepted 22 August 2009
Available online 3 September 2009

*Keywords:*
Multiphase flow
Lattice-Boltzmann
Interfacial area
Capillary pressure
Porous media
Computed microtomography

ABSTRACT

Hysteresis in the relationship between capillary pressure ($P_c$), wetting phase saturation ($S_w$) and nonwetting–wetting interfacial area per volume ($a_{nw}$) is investigated using multiphase lattice-Boltzmann simulations of drainage and imbibition in a glass bead porous system. In order to validate the simulations, the $P_c$—$S_w$ and $a_{nw}$—$S_w$ main hysteresis loops were compared to experimental data reported by Culligan et al. [Culligan KA, Wildenschild D, Christensen BS, Gray WG, Rivers ML, Tompson AB. Interfacial area measurements for unsaturated flow through porous media. Water Resour Res 2004;40:W12413]. In general, the comparison shows that the simulations are reliable and capture the important physical processes in the experimental system. $P_c$—$S_w$ curves, $a_{nw}$—$S_w$ curves and phase distributions (within the pores) show good agreement during drainage, but less satisfactory agreement during imbibition. Drainage and imbibition scanning curves were simulated in order to construct $P_c$—$S_w$—$a_{nw}$ surfaces. The root mean squared error (RMSE) and mean absolute error (MAE) between drainage and imbibition surfaces was 0.10 $mm^{-1}$ and 0.03 $mm^{-1}$, respectively. This small difference indicates that hysteresis is virtually nonexistent in the $P_c$—$S_w$—$a_{nw}$ relationship for the multiphase system studied here. Additionally, a surface was fit to the main loop (excluding scanning curves) of the drainage and imbibition $P_c$—$S_w$—$a_{nw}$ data and compared to the surface fit to all of the data. The differences between these two surfaces were small (RMSE = 0.05 $mm^{-1}$ and MAE = 0.01 $mm^{-1}$) indicating that the $P_c$—$S_w$—$a_{nw}$ surface is adequately represented without the need for the scanning curve data, which greatly reduces the amount of data required to construct the non-hysteretic $P_c$—$S_w$—$a_{nw}$ surface for this data.

© 2009 Elsevier Ltd. All rights reserved.

## 1. Introduction

Classical macro-scale multiphase flow models rely heavily on extensions of Darcy's law and empirical relationships that do not fully capture all of the important physical phenomena of such multiphase systems [1]. For example, a common approach used to model two-phase flow of air–water or NAPL–water systems in subsurface environments is to model each phase separately using Darcy's law and account for the interaction between the fluids by (1) introducing a relative permeability term and by (2) assuming the pressure gradients between the two phases are related by $P_c$ [2]. This approach does not explicitly account for fluid–fluid interfaces and the result is a relationship in which the macroscopic capillary pressure is assumed to be a function of $S_w$ only [3,4]. Additionally, the traditional $P_c$—$S_w$ relationship assumes that, at static conditions, $P_c$ is uniquely described by $S_w$; nevertheless, many different pore-scale fluid configurations can correspond to a given $S_w$ [5]. This suggests that in addition to saturation, a macro-scale variable that accounts for multiple pore-scale fluid configurations is required to accurately characterize multiphase systems.

Based on thermodynamic considerations, Hassanizadeh and Gray [8,9] developed a multiphase flow theory that includes the conservation of mass, momentum and energy at the interfaces between phases. Within their theory they proposed a constitutive relationship between $P_c$—$S_w$—$a_{nw}$, in which the interfaces between phases are explicitly taken into account and the pore-scale fluid configuration is quantified by $a_{nw}$. Experimental validation of this theory is currently of great interest. Culligan et al. [6,7] used computed microtomographic (CMT) image data from drainage and imbibition experiments to estimate interfacial area per volume. The data collected in these investigations was found to be consistent with the theory presented by Hassanizadeh and Gray [8,9], however, due to the lack of scanning curves, no attempt was made to investigate the uniqueness of the $P_c$—$S_w$—$a_{nw}$ relationship. Cheng et al. [10] estimated $a_{nw}$ for a 2D synthetic porous medium and concluded that $a_{nw}$ lifts the ambiguity associated with the hysteretic nature of the $P_c$—$S_w$ relationship.

* Corresponding author. Tel.: +1 541 517 2761.
*E-mail address:* porterma@engr.orst.edu (M.L. Porter).

0309-1708/$ - see front matter © 2009 Elsevier Ltd. All rights reserved.
doi:10.1016/j.advwatres.2009.08.009

Author's personal copy



In addition to experimental work, pore-scale modeling techniques have been used to estimate $a_{nw}$ [11,12] and investigate the $P_c$—$S_w$—$a_{nw}$ relationship [13–17]. Reeves and Celia [13] developed a pore network model consisting of spherical pore bodies and biconical throats, and concluded that the capillary pressure showed a strong dependence on the interfacial area between the fluid phases. Moreover, they observed notable differences between the drainage and imbibition $P_c$—$S_w$—$a_{nw}$ surfaces. Held and Celia [14] developed a pore network model that included a snap-off mechanism and the resulting $P_c$—$S_w$—$a_{nw}$ surface enclosed in the main hysteresis loop exhibited a pronounced concave curvature, thus $P_c = f(S_w, a_{nw})$ was not single valued; moreover, they observed that $a_{nw} = f(S_w, P_c)$ was single valued and may be a preferable functional form. Joekar-Niasar et al. [16] recently developed a pore network model and found that hysteresis was minimal in $P_c$—$S_w$—$a_{nw}$ when the pore size distribution included a significant proportion of overlapping pore bodies and pore throats. Additionally, Helland and Skjaeveland [17] demonstrated that hysteresis does exist in the $P_c$—$S_w$—$a_{nw}$ relationship for a mixed-wet porous system comprised of triangular capillary tubes. From this brief review it is clear that no definitive conclusions have been drawn from current experimental and numerical studies regarding the functional relationship of $P_c$—$S_w$—$a_{nw}$, thus further study is warranted.

Numerous authors have shown that lattice-Boltzmann (LB) models are capable of simulating three-dimensional multiphase and multi-component fluid flow in complex porous systems (e.g., [18–26]), however, to the best of our knowledge, no LB numerical studies have been presented in the literature that address $a_{nw}$—$S_w$ curves or the $P_c$—$S_w$—$a_{nw}$ relationship. Accordingly, the objective of this study is to conduct LB simulations of drainage and imbibition in a realistic porous medium in order to investigate hysteresis in the $P_c$—$S_w$—$a_{nw}$ relationship. In Section 2.1 we briefly describe some of the components of the Shan and Chen type (hereafter, SC type) two-component model [27,28,18] that was used for the simulations in this study. Section 2.2 describes the details regarding the LB simulations and the analysis required to obtain interfacial area estimates. In Section 3, we present the results and discussion for $P_c$—$S_w$ curves, phase distributions within the pores, $a_{nw}$—$S_w$ curves and the $P_c$—$S_w$—$a_{nw}$ relationship. The discussion regarding the $P_c$—$S_w$ curves, phase distributions, and the $a_{nw}$—$S_w$ curves, focuses on comparisons between the simulations and experimental results presented by Culligan et al. [6] for the main hysteresis loops. The comparisons serve as a validation of the main hysteresis loops and justification of the simulated scanning curves required to investigate hysteresis in the $P_c$—$S_w$—$a_{nw}$ relationship. Finally, the summary and general conclusions are presented in Section 4.

## 2. Numerical methods

### 2.1. Lattice-Boltzmann model

The LB method was chosen for this study over other pore-scale modeling techniques (e.g., pore network) because of the availability of high resolution CMT image data, which defines the pore geometry in the simulations. The fundamental idea behind the LB modeling technique is the construction of simplified kinetic models that incorporate the essential physics of the microscopic processes such that the macroscopic averaged properties obey the desired macroscopic equations, in this case the Navier–Stokes equations [29]. A full description of the LB model used in this study is beyond the scope of this work and we refer the reader to Schaap et al. [25] for details. In the multi-component SC type model, interaction between phases, namely the fluid–fluid cohesive force and fluid–solid adhesive force, is taken into account phenomenologically by modifying the macroscopic momentum variable.

The fluid–fluid cohesive force is calculated based on the presence of the other fluid in neighboring lattice sites and is given as:

$$\mathbf{F}_{c,\alpha,\alpha'}(\mathbf{x}) = -n_\alpha(\mathbf{x}) \sum_i^{18} G_{c,\alpha} n_{\alpha'}(\mathbf{x} + \mathbf{e}_i)\mathbf{e}_i, \quad \alpha \neq \alpha', \tag{1}$$

where $n_\alpha(\mathbf{x})$ is the number density, $G_{c,\alpha}$ is the fluid–fluid interaction potential, the vector $\mathbf{e}_i$ accounts for the relative position of neighboring lattice sites, and the subscripts $\alpha$ and $\alpha'$ denote different components. It is the fluid–fluid cohesive force that gives rise to surface tension. The value of $G_{c,\alpha}$ is positive and identical for both fluid components and the choice of $G_{c,\alpha}$ determines the nature of the interaction between the two fluids; smaller values lead to unsharp interfaces and a considerable amount of diffusion from one component into the other, whereas larger values lead to sharp interfaces and purer component mixtures.

The fluid–solid adhesive force is determined by the presence of the solid phase at neighboring lattice sites and is given as:

$$\mathbf{F}_{a,\alpha}(\mathbf{x}) = -n_\alpha(\mathbf{x}) \sum_i^{18} G_{a,\alpha} s(\mathbf{x} + \mathbf{e}_i)\mathbf{e}_i, \tag{2}$$

where $G_{a,\alpha}$ is the fluid–solid interaction potential and $s(\mathbf{x} + \mathbf{e}_i)$ is an indicator function that is 1 and 0 for solid and fluid lattice sites, respectively. In this model $G_{a,1} = -G_{a,2}$ where $G_{a,1}$ is the interaction potential for the nonwetting phase and $G_{a,2}$ is the interaction potential for the wetting phase.

The choice of $G_{a,\alpha}$ along with $G_{c,\alpha}$ determines the contact angle, which are generally determined via simulation. Schaap et al. [25] performed bubble and tube simulations to obtain values for $G_{c,\alpha}$ and $G_{a,\alpha}$. The bubble simulations indicated that $G_{c,\alpha} = 0.025$ was a suitable choice for the applications in this study. The lattice surface tension, $\sigma^*$, was determined by combining bubble simulations with Laplace's law to obtain $\sigma^* = 0.1773$. The tube simulations indicated that $G_{a,\alpha} = 0.0120$ corresponded to a 0° contact angle; however, it has since been proposed that $G_{a,\alpha}$ may be determined *a priori* using the Young–Laplace equation [30]. Using LB parameters the Young–Laplace equation takes the following form:

$$\cos(\theta) = \frac{G_{a,1} - G_{a,2}}{G_c}, \tag{3}$$

where $\theta$ is the contact angle. Since $G_{a,1} = -G_{a,2}$, Eq. (3) reduces to $\cos(\theta) = 2G_{a,1}/G_c$ and one can easily show that $G_{a,1} = 0.0125$ and $G_{a,2} = -0.0125$ for a contact angle of 0° and $G_c = 0.025$. The values of $G_{a,\alpha}$ as determined by Eq. (3) was used in the simulations presented in this study, which is slightly different than the value obtained from the tube simulations used in previous simulations [25].

### 2.2. LB simulations

Fig. 1 is an illustration of both the experimental and simulated systems, which shows that the simulated system is a small section of the experimental system. This difference has implications for the LB simulations since it is not possible to exactly match the boundary conditions in the two systems. In the LB simulations, the boundary conditions are applied at the top and bottom of the imaged section of the porous medium, whereas in the experiments the boundary conditions are at the inlet and outlet of the column. In addition, the computational demands required for each LB simulation were too great to conduct the simulations at the resolution of the CMT image data (17 μm). Thus, the experimental CMT images were binned to reduce the size of the lattice. The binning step consisted of combining a cube of 8 voxels into 1 voxel, thus reducing the lattice size from 410 × 410 × 300 voxels (17 μm resolution) to 205 × 205 × 150 voxels (34 μm resolution).

Author's personal copy



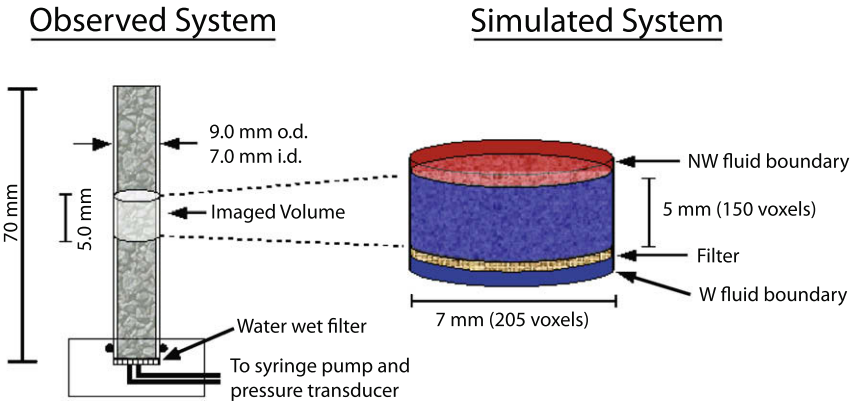


**Fig. 1.** Illustration of the experimental system and the portion of the sample modeled in the LB simulations.

The total model domain consists of a cubic lattice that is $207 \times 207 \times 166$, which is larger than the porous medium on the sides and ends of the imaged porous medium. The lattice exceeds the diameter of the cylinder by two pixels to preserve the solid boundaries of the cylinder, allowing for the use of the standard "bounce back" algorithm at the column boundaries. A hydrophilic semi-permeable layer consisting of equally spaced fluid pores (1 voxel each) surrounded by solid voxels is included in the lattice at the bottom of the porous medium to simulate the semi-permeable membrane used in the experimental system. Additionally, a buffer of eight fluid layers were included at the top (nonwetting) and bottom (wetting) boundaries of the lattice (see Fig. 1).

Dimensional analysis [6,25] indicated that the dominating force in the experimental system was capillarity. Based on these findings, the effects of gravity were not considered in the simulations, and the density and viscosity ratios between the simulated fluids were set to one, greatly reducing the computational complexity of the model system.

In this study two different types of simulations are presented. In the first type of simulations, flux boundary conditions were used at the inlet and outlet boundaries. In the second type of simulations, constant pressure boundary conditions were used at the inlet and outlet. Hereafter, the two types of simulations will be referred to as flux simulations and pressure simulations.

The experiments consisted of pumping a precise amount of water at a specified flow rate into (or out of) the system and then allowing the system to equilibrate. In the flux simulations, a flux boundary condition was used to simulate the pumping of wetting fluid into and out of the porous medium. The flux boundary conditions were determined by scaling the characteristic flow rate from the experimental system using the Reynolds number:

$$Re = Re^* \rightarrow \frac{u_w R_{char}}{\phi v_w} = \frac{u^* R^*_{char}}{\phi^* v^*}, \tag{4}$$

where $u$ is the Darcy velocity, $R_{char}$ is the characteristic pore radius, $\phi$ is the porosity, $v$ is the kinematic viscosity and the superscript $^*$ indicates lattice parameters. It is $u^*$ that was used as the flux at each boundary node, which was set to 0.00008 mass units per time step (mu ts$^{-1}$), corresponding to a Darcy flow velocity of 0.014 mm/s. At a flux of 0.00008 mu ts$^{-1}$, approximately 50,000 ts were required to obtain a 5% change in saturation, which took about 1.25 days to run in parallel on four amd64 CPU (2.8 GHz) machines for a lattice domain of $207 \times 207 \times 166$ voxels.

The flux simulations were conducted in sequence starting from a fully saturated porous medium. The final fluid distributions and capillary pressures from each simulation were used as the initial condition for subsequent simulations. In each simulation, a prescribed amount of fluid was allowed to drain or imbibe into the porous medium at a flux of 0.00008 mu ts$^{-1}$ followed by a period in which the flux was set to zero, allowing the system to equilibrate. In this fashion primary drainage, main imbibition and main drainage curves were simulated in succession. Additionally, numerous imbibition and drainage scanning curves were simulated using points from the $P_c$—$S_w$ main hysteresis loop as the initial condition.

The motivation for the pressure simulations was to investigate the difference in results using different boundary conditions and different wetting/drying histories. Additionally, the standard method for determining $P_c$—$S_w$ curves in the laboratory is to employ constant pressure boundary conditions at the inlet and outlet of the column. In these simulations, a constant pressure was prescribed at each of the boundaries. The prescribed boundary conditions were determined from duct simulations, see Schaap et al. [25]. The pressure simulations were conducted as single step drainage and imbibition simulations, which consisted of starting each simulation from a completely saturated (drainage) or dry (imbibition) porous medium. By conducting single step simulations, all of the points on the curve were simulated simultaneously, reducing the total amount of time to obtain the drainage and imbibition curves. Thus, in these simulations primary drainage and primary imbibition curves were obtained.

Estimates of saturation and interfacial area per volume were of primary interest in this study and additional analysis was required to obtain this information from both the CMT and LB data. Due to differences in the data format, slightly different analysis methods were required. The CMT data consists of gray scale intensity values that were segmented using a $k$-means cluster analysis (see [31] for complete details). The segmented data consisted of ternary data with each phase represented by a single integer value, which was used to estimate the porosity and saturation by counting voxels. The LB data did not require segmentation since the solid phase was pre-defined and a smooth gradient exists between the wetting and the nonwetting phases. The saturation was simply determined from component densities using the following rule: if the nonwetting component density was greater than or equal to the wetting component density at a given lattice site, then the lattice site was considered to be nonwetting phase, otherwise it was wetting phase. Interfacial area estimates were obtained using Avizo$^{TM}$ for both the experimental and LB data. This software uses a generalized marching cubes algorithm to generate isosurfaces from which interfacial area is estimated. In Porter and Wildenschild [31] we compared interfacial area estimates using this approach and other approaches based on marching cubes algorithms (including the porous medium marching cubes (PMMC) algorithm recently developed by McClure et al. [32]). Our results for nonwetting–wetting

Author's personal copy



phase interfaces contained within capillary tubes showed that the interfacial area estimates for all approaches (based on marching cubes algorithms) were within 15% error of the analytical estimate.

## 3. Results and discussion

### 3.1. Equilibrium validation

In the LB simulations it was assumed that equilibrium was obtained when the change in capillary pressure (for the flux simulations) and the change in saturation (for the pressure simulations) over time became negligible. Thus, the change in $P_c$ and the change in $S_w$ for the last 10,000 ($\Delta P_c^{10,000}$ and $\Delta S_w^{10,000}$) iterations was estimated for all simulations. The values for $\Delta P_c^{10,000}$ ranged from 0 to 0.25 Pa for all simulations, which represents less than 1% change in $P_c$ near the end of these simulations. The values for $\Delta S_w^{10,000}$ ranged from 0 to 0.00012. Based on this analysis it was assumed that all simulations had reached equilibrium.

### 3.2. Capillary pressure–saturation curves

$P_c$—$S_w$ curves for the experiments and both sets of simulations are presented in Fig. 2. It is emphasized that the comparison serves as a validation of the simulations, rather than a prediction of the experimental observations, since the simulations correspond to a geometry that is coarser than the experimental images, and it was not possible to match the boundary conditions of the experiments (see discussion in Section 2.2). With this in mind, the comparison between the experimental and both simulated drainage curves is promising. The nonwetting phase entry pressures for the primary drainage simulations are lower than observed in the experimental primary drainage curve. Relatively good agreement is observed for all drainage simulations and the secondary drainage experiments, which is encouraging considering the differences between the two systems.

During the flux simulations, at high $P_c$ values, the nonwetting phase broke through the hydrophilic semi-permeable layer that was implemented at the bottom of the porous medium, thus the lack of data points for $S_w < 0.15$ in Fig. 2a. Breakthrough of the nonwetting phase in the flux simulations was most likely due to dynamic effects (i.e., increased pressure and interfacial curvature due to fluid flow).

In the flux simulations (Fig. 2a), imbibition was initiated at the final drainage point on the $P_c$—$S_w$ curve, whereas for the pressure simulations (Fig. 2b) imbibition was initiated from a fully drained porous medium. In both cases, Fig. 2 indicates that the imbibition simulations do not correspond to the experimental imbibition curves at low $S_w$ values; however at $S_w > 0.45$ the correspondence between the experimental and simulated imbibition curves is good, especially for the flux simulations. The discrepancy at low $S_w$ values is, in part, due to the coarsening of the lattice in the binning step, which altered the geometry of the porous medium, especially the smallest pores and throats. Additionally, during imbibition there was increased spreading of the wetting phase in the corners of the digitized images near all solids, thus increasing film flow in the imbibition simulations. Moreover, the size of the films in the simulations is 34 μm (since that is the voxel resolution), which is much greater than the physical films in the experimental system. Ahrenholz et al. [26] discuss the existence of unphysical films in LB simulations based on CMT data.

### 3.3. Phase distributions

Figs. 3 and 4 compare vertical cross sections of the fluid distributions for various saturations during drainage and imbibition, respectively. The saturations in each column were matched as closely as possible, but in some cases this was not possible since the simulations were not controlled for saturation; for this reason no attempt was made to quantify the differences between the phase distributions presented. Fig. 3 shows that, qualitatively, the fluid distributions for drainage are in good agreement for all three systems. This result is somewhat unexpected since the boundary conditions in each system are different. Additionally, the fluid–fluid and fluid–solid interactions in the LB model are incorporated phenomenologically, yet the overall distribution of fluid phases at equilibrium is captured. During imbibition, see Fig. 4, it is evident that there is less agreement between the simulated and experimental fluid distributions. A large nonwetting phase ganglia exists in the upper right hand corner of the experimental images (row 1) for all $S_w$ values for imbibition, whereas, in the imbibition simulations this nonwetting phase blob is not present at higher $S_w$ values. This is in part due to the differences between the boundary conditions between the experiments and simulations for the imaged section.

### 3.4. Interfacial area–saturation curves

Drainage and imbibition $a_{nw}$—$S_w$ curves are presented in Fig. 5 and are represented by the open and solid symbols, respectively. Fig. 5 shows that there is very good agreement between the exper-

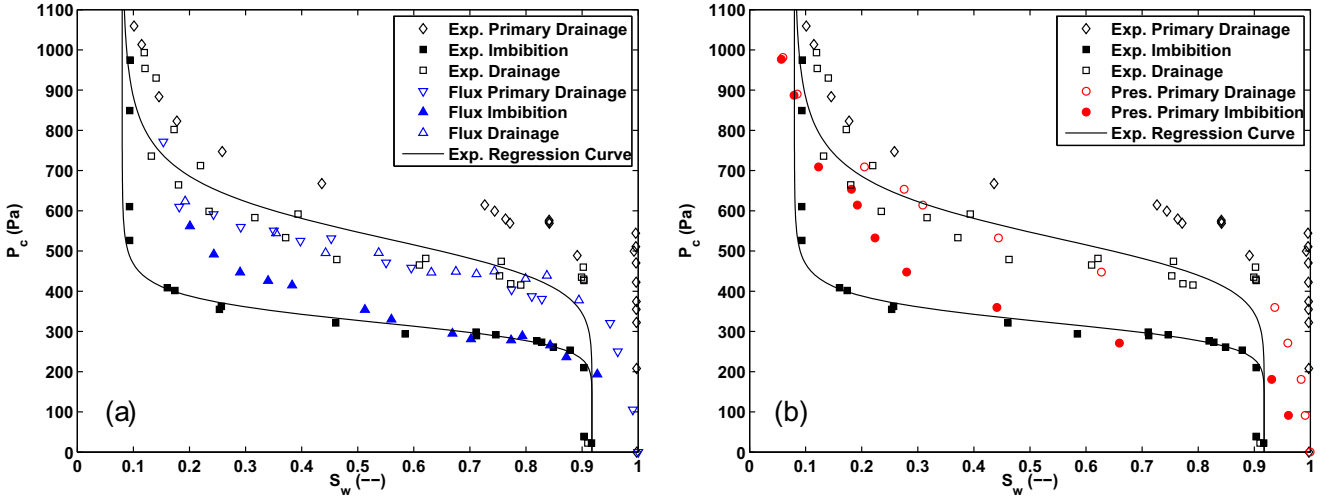


**Fig. 2.** Comparison of the $P_c$—$S_w$ curves obtained from the experiments with (a) the flux and (b) the pressure LB simulations.

Author's personal copy



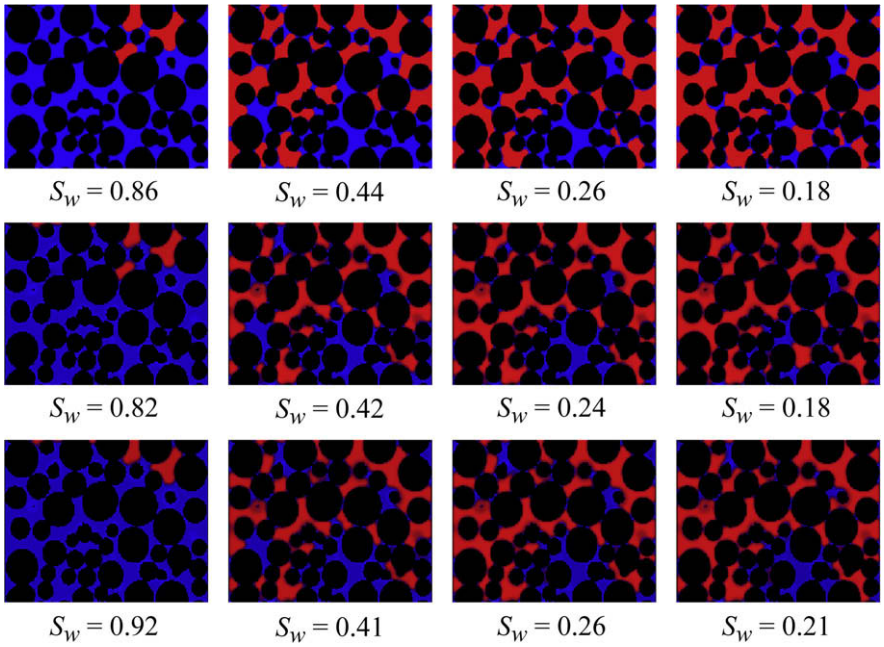


**Fig. 3.** Comparison between fluid distributions of the experimental segmented data (1st row), flux simulations (2nd row) and pressure simulations (3rd row) at various saturations during *drainage* for a vertical cross section where red and blue are the nonwetting and wetting fluids, respectively. (For interpretation of the references to color in this figure legend, the reader is referred to the web version of this article.)

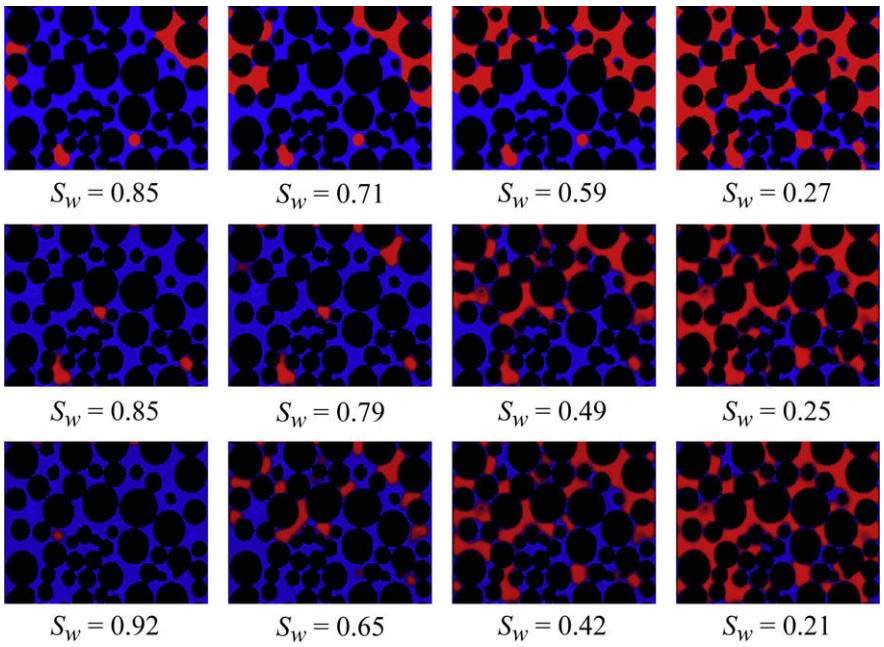


**Fig. 4.** Comparison between fluid distributions of experimental segmented data (1st row), flux simulations (2nd row) and pressure simulations (3rd row) at various saturations during *imbibition* for a vertical cross section where red and blue are the nonwetting and wetting fluids, respectively. (For interpretation of the references to color in this figure legend, the reader is referred to the web version of this article.)

imental drainage data and both drainage simulations. Furthermore, there is little difference between the primary drainage and main drainage for the flux simulations, which is consistent with the experimental data. Network modeling results presented by Held and Celia [14] and Reeves and Celia [13], however, predict primary drainage $a_{nw}$–$S_w$ curves that are lower than the corresponding main drainage curve.

The simulated imbibition curves in Fig. 5 are considerably higher than the experimental imbibition data. The LB modeling results for imbibition are consistent with LB results presented by McClure et al. [33] and network modeling results presented by Held and Celia [14] and Joekar-Niasar et al. [16], in that these numerical investigations resulted in higher $a_{nw}$ during main imbibition than in primary drainage. Reeves and Celia [13], on the other hand, reported $a_{nw}$ values that cross during primary drainage and main imbibition. In the $a_{nw}$–$S_w$ LB simulation curves presented in this study the unexpected high values of $a_{nw}$ during imbibition are, in part, due to increased spreading of the wetting phase and the

Author's personal copy



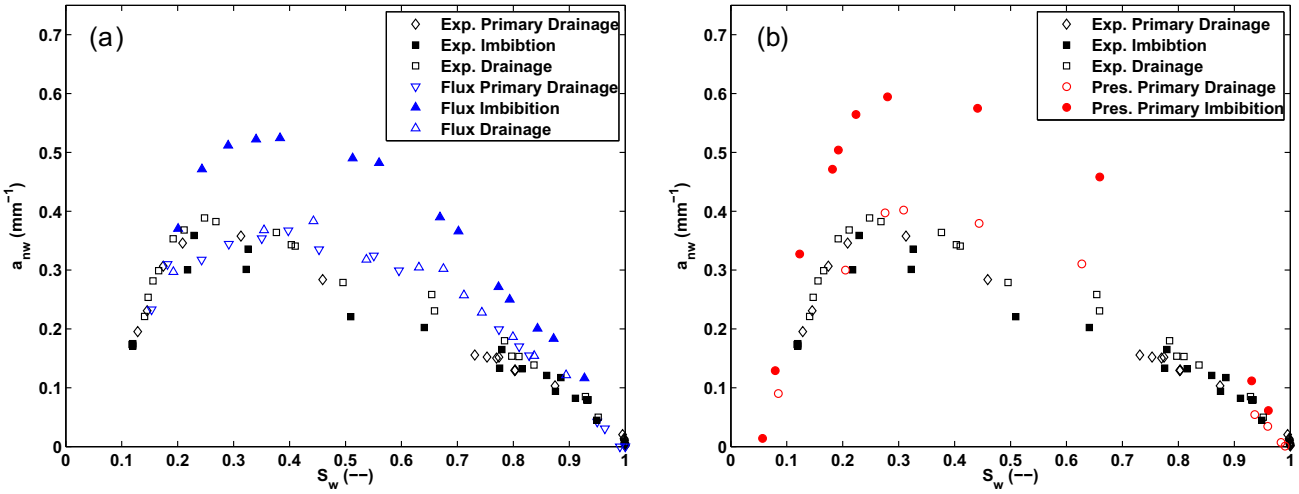


**Fig. 5.** Comparison of the $a_{nw}$–$S_w$ curves obtained from the experiments and (a) flux and (b) pressure LB simulations. The open symbols represent drainage, whereas the solid symbols represent imbibition.

unphysical size (34 μm) of the wetting phase films (as discussed in Section 3.2). Additionally, the differences in the morphology of the disconnected nonwetting phase significantly affects $a_{nw}$ values. In the LB simulations the nonwetting phase morphology consisted of many small disconnected blobs which have a high interfacial area to volume ratio; whereas in the experimental system the nonwetting phase morphology primarily consisted of a few large ganglia (see Fig. 4), which have a small interfacial area to volume ratio.

### 3.5. Capillary pressure–saturation–interfacial area relationship

Fig. 6 shows the $P_c$–$S_w$ and $a_{nw}$–$S_w$ scanning curves that were simulated in order to investigate the $P_c$–$S_w$–$a_{nw}$ relationship. Both imbibition and drainage scanning curves were simulated using points from the main hysteresis loop (flux LB simulations) as the initial condition. The scanning curves are bounded by the main hysteresis loop for both $P_c$–$S_w$ and $a_{nw}$–$S_w$, as expected. The combination of $P_c$–$S_w$ and $a_{nw}$–$S_w$ data for the flux LB simulations yields physically consistent hysteresis loops and scanning curves, allowing us to analyze the data in three dimensions. For this analysis, we have chosen to use $a_{nw} = f(S_w, P_c)$ rather than $P_c = f(S_w, a_{nw})$ since we observed that our $P_c = f(S_w, a_{nw})$ data has a distinct concave curvature and is not single valued (not shown here), and similar findings have been reported in the literature (e.g. [13,14,16]). To this end, surfaces were fit to the $P_c$–$S_w$–$a_{nw}$ simulation data using a bi-quadratic equation of the following form

$$a_{nw}(S_w, P_c) = AP_c^2 + BP_c + CP_cS_w + DS_w + ES_w^2 + F, \quad (5)$$

where $A, B, C, D, E$, and $F$ are best-fit parameters. We have chosen this equation because of its simplicity and we note that Joekar-Niasar et al. [16], Niessner and Hassanizadeh [34,35] use a similar equation. We realize that Eq. (5) is an empirical equation that does not account for all of the system's physical constraints and we are currently exploring alternative expressions that address this issue.

A total of four surfaces were fit to the $P_c$–$S_w$–$a_{nw}$ data, which included one surface for the main branches and scanning curve data for drainage (hereafter, Drainage Surface), one surface for the main branch and scanning curve data for imbibition (hereafter, Imbibition Surface) one surface for all of the $P_c$–$S_w$–$a_{nw}$ data (i.e., all of the data presented in Fig. 6) (hereafter, Unique Surface), and one surface for the drainage and imbibition main hysteresis loop data (hereafter, Main Loop Surface). For all four surfaces the correlation coefficient was 0.99, indicating that Eq. (5) adequately

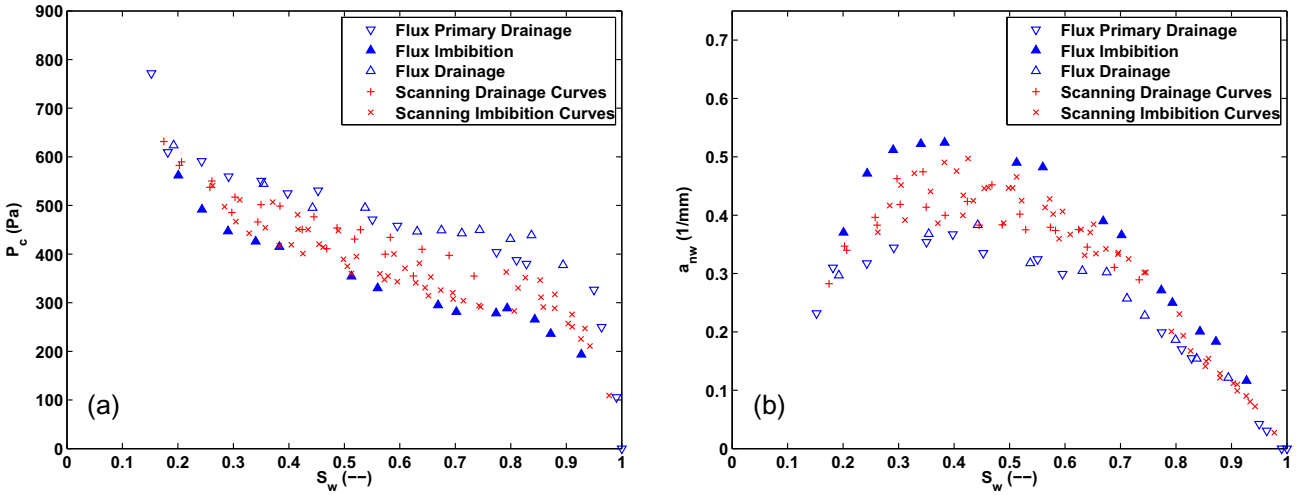


**Fig. 6.** Drainage (+) and imbibition (×) scanning curves for (a) $P_c$–$S_w$ and (b) $a_{nw}$–$S_w$. This data was obtained using only the flux simulations.

Author's personal copy



**Table 1**
Best-fit coefficients for Eq. (5).

| | A | B | C | D | E | F |
|---|---|---|---|---|---|---|
| Drainage Surface | 5.2925e−07 | −0.0026 | 0.0024 | −1.5086 | −0.2265 | 1.7355 |
| Imbibition Surface | −1.9086e−07 | −0.0019 | 0.0018 | −1.1412 | −0.3725 | 1.5346 |
| Unique Surface | 4.0391e−07 | −0.0024 | 0.0022 | −1.2413 | −0.3405 | 1.5956 |
| Main Loop Surface | 2.3945e−07 | −0.0024 | 0.0023 | −1.3726 | −0.3044 | 1.6817 |

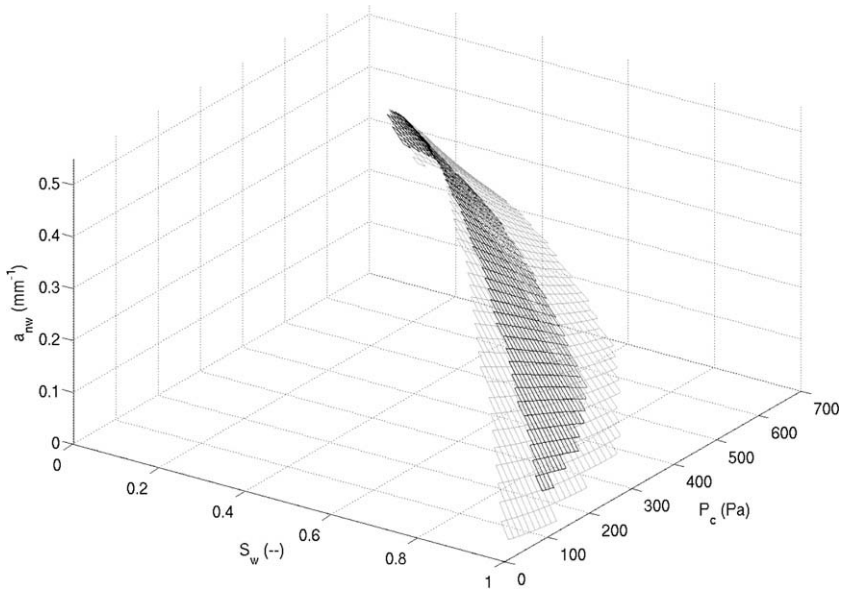


**Fig. 7.** Separate drainage (gray) and imbibition (black) best-fit surfaces of the $P_c$—$S_w$—$a_{nw}$ data.

**Table 2**
The root mean squared error (RMSE) and mean absolute error (MAE) for $P_c$—$S_w$—$a_{nw}$ surface pairs. Units are in mm$^{-1}$.

| | RMSE | MAE |
|---|---|---|
| Drainage Surface/Imbibition Surface | 0.10 | 0.03 |
| Unique Surface/Drainage Surface | 0.09 | 0.02 |
| Unique Surface/Imbibition Surface | 0.08 | 0.03 |
| Main Loop Surface/Unique Surface | 0.05 | 0.01 |

represents the data. The values for the best-fit parameters for each surface using a least-squares algorithm are shown in Table 1.

First, we estimated hysteresis between the Drainage Surface and the Imbibition Surface (see Fig. 7) by calculating the root mean squared error (RMSE) and mean absolute error (MAE) for the two surfaces. Table 2 (row 1) shows that the difference between the two surfaces is negligible. This suggests that both the drainage and imbibition data can be described by a single, unique surface (see Fig. 8). The RMSE and MAE was calculated between the Unique Surface and both the Drainage and Imbibition Surfaces (see Table 2, rows 2 and 3). The results indicate that the Unique Surface is not significantly different than either of the Drainage or Imbibition Surfaces. Thus, the analysis suggests that the LB $P_c$—$S_w$—$a_{nw}$ data is single valued and hysteresis is virtually nonexistent, which supports the theory proposed by Hassanizadeh and Gray [8,9]. It is necessary to point out that the apparent trends in the two-dimensional projections of $P_c$—$S_w$ and $a_{nw}$—$S_w$ shown in Figs. 2 and 5 should be interpreted with regards to the missing variable.

In general, it is expensive and difficult to measure or simulate the necessary scanning curves to construct the $a_{nw} = f(S_w, P_c)$ surface. Thus, it is desirable to be able to construct the $a_{nw} = f(S_w, P_c)$ surface with the least amount of data possible. Since the main hysteresis loop (i.e., excluding scanning curves) is typically measured or simulated for multiphase flow modeling, the Main Loop Surface was fit to this data, see Fig. 9. We compared the Main Loop Surface to the Unique Surface and the RMSE and MAE (see Table 2, row 4) indicate that there is no significant difference between the two surfaces. This implies that, for this system, a representative $a_{nw} = f(S_w, P_c)$ surface is obtained without the need for scanning curves, a result which has significant practical implications.

## 4. Summary and conclusions

In this study an LB model was used to simulate drainage and imbibition processes and estimate interfacial area per volume for the nonwetting–wetting interface ($a_{nw}$) from the resulting $P_c$—$S_w$ data. The simulation data was validated by a comparison with the experimental observations reported by Culligan et al. [6]. The pore geometry from the experimental CMT image data was used to define the porous medium in the simulations, however it was necessary to coarsen the experimental CMT image data by a factor of 2 in order to simulate the full experimental domain and reduce computational demands for the LB simulations. Two different types of simulations, namely flux and pressure simulations, were developed and compared to the experimental data. The flux simulations consisted of flux boundary conditions at the inlet and outlet of the column and multiple drainage and imbibition steps were simulated in succession. The pressure simulations consisted of multiple single step drainage and imbibition events starting from a fully saturated or fully drained porous medium, and pressure boundary conditions were used at the inlet and outlet.

A comparison between the experimental and simulated $P_c$—$S_w$ and $a_{nw}$—$S_w$ main hysteresis loops served as a validation of the

Author's personal copy



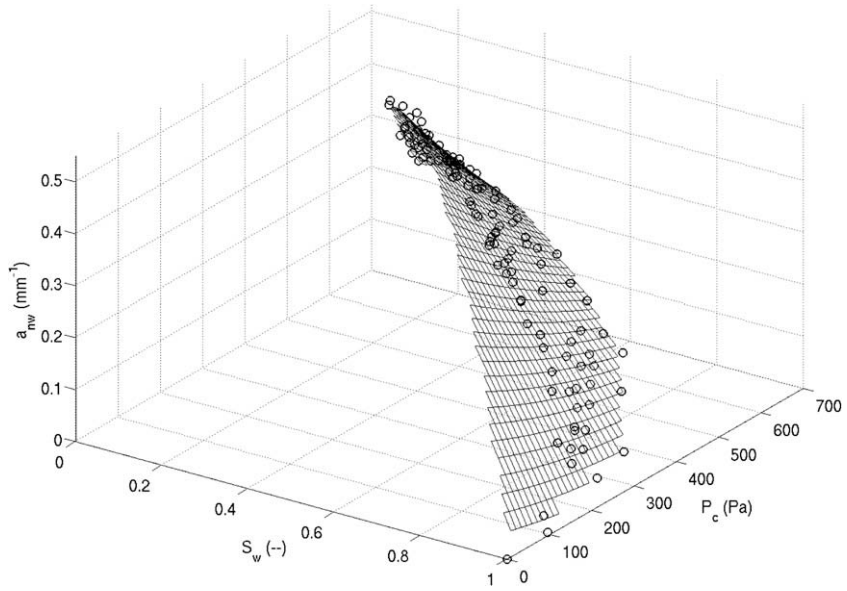


**Fig. 8.** Best-fit surface of the complete $P_c$–$S_w$–$a_{nw}$ data set.

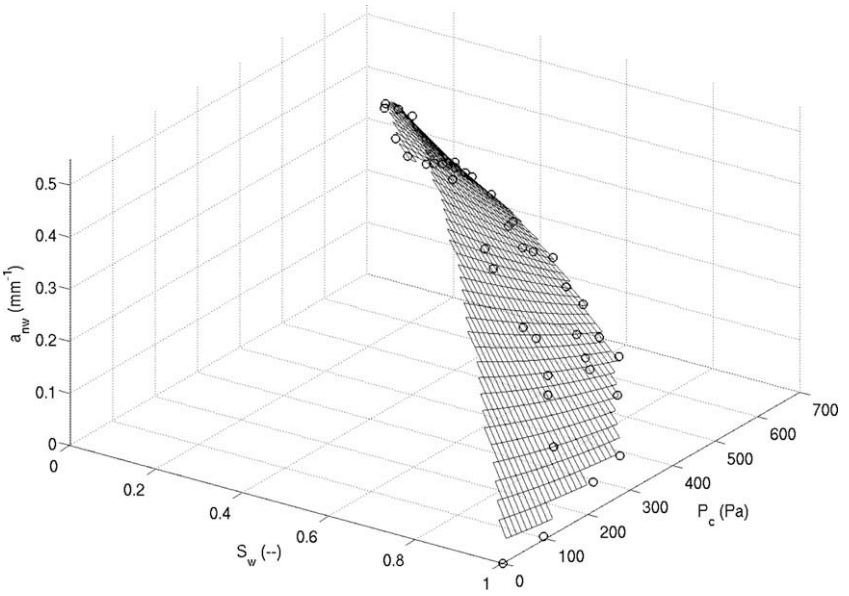


**Fig. 9.** Best-fit surface of the $P_c$–$S_w$–$a_{nw}$ main hysteresis loop data.

modeling results. In general the comparison showed that the main hysteresis loops for $P_c$–$S_w$ and $a_{nw}$–$S_w$ were realistic and justified additional scanning curve simulations. The most notable discrepancies in the main hysteresis loops occurred at low $S_w$ values for the $P_c$–$S_w$ imbibition curves and for imbibition in the $a_{nw}$–$S_w$ curves. At low $S_w$ values the nonwetting phase fluid broke through the artificial hydrophilic semi-permeable layer at the bottom of the column, which prevented flux simulations for $S_w < 0.15$. Neither of the simulated $P_c$–$S_w$ imbibition curves matched the experiments well at low saturations, but tended to agree at higher saturations. Considering the complexity of the processes involved, the model generally matched the experiments rather well, especially with regards to the fluid configurations within the pores during drainage. The comparison between $a_{nw}$–$S_w$ curves showed good agreement for drainage, however, the simulated imbibition curves were higher than observed in the experiments. We argue that this discrepancy is in part due to unphysical spreading of the wetting phase during imbibition leading to increased film flow; moreover, the films in the LB simulations are 34 μm, whereas in the experimental system they are much smaller. Additionally, it was argued that differences in the morphology of the disconnected nonwetting phase also caused some of the discrepancies observed in the imbibition $a_{nw}$–$S_w$ curves. A review of the literature suggested that the simulated $a_{nw}$–$S_w$ curves presented here are consistent with those obtained from other numerical studies, in that the main imbibition $a_{nw}$–$S_w$ curve was greater than the primary drainage curve.

The uniqueness of the $P_c$–$S_w$–$a_{nw}$ relationship proposed by Hassanizadeh and Gray [8,9] was investigated using the main hysteresis loop of the flux simulations and numerous scanning curves to create a surface in three dimensions. Based on this data, a biquadratic equation was fit to the $P_c$–$S_w$–$a_{nw}$ data. The functional dependence was chosen to be $a_{nw} = f(S_w, P_c)$ rather than $P_c = f(S_w, a_{nw})$ since we observed that our $P_c = f(S_w, a_{nw})$ data has a distinct concave curvature and is not single valued. The RMSE

Author's personal copy



and MAE between (1) the Drainage and Imbibition Surfaces and (2) the Unique Surface and both the Drainage and Imbibition Surfaces were small suggesting that the hysteresis was negligible in the simulated system. Moreover, it was shown that the surface created using only the hysteresis loop data (Main Loop Surface) was very similar to the Unique Surface, suggesting that it is possible to construct a non-hysteretic $P_c$—$S_w$—$a_{nw}$ surface without the need for the scanning curve data, which is of great interest since the amount of data required for the surface is greatly reduced.

## Acknowledgments

Porter and Wildenschild were supported, in part, by NSF-EAR-06101108 and NSF-EAR-0337711. Schaap was supported, in part, by NSF-EAR-0337378 and NSF-EAR-061003. A portion of this work was conducted at GeoSoilEnviroCARS (Sector 13), Advanced Photon Source (APS), Argonne National Laboratory. GeoSoilEnviroCARS is supported by the National Science Foundation – Earth Sciences (EAR-0622171) and Department of Energy – Geosciences (DE-FG02-94ER14466). Use of the Advanced Photon Source was supported by the US Department of Energy, Office of Science, Office of Basic Energy Sciences, under Contract No. DE-AC02-06CH11357.

## References

[1] Muccino JC, Gray WG, Ferrand LA. Toward an improved understanding of multiphase flow in porous media. Rev Geophys 1998;36(3):401–22.
[2] Dullien FAL. Porous media: fluid transport and pore structure. 2nd ed. Academic Press; 1992.
[3] Bear J. Dynamics of fluids in porous media. Dover Publications, Inc.; 1988.
[4] Hassanizadeh MS, Celia MA, Dahle HK. Dynamic effect in the capillary pressure–saturation relationship and its impacts on unsaturated flow. Vadose Zone J 2002;1:38–57.
[5] Gray WG, Hassanizadeh MS. Paradoxes and realities in unsaturated flow theory. Water Resour Res 1991;27(8):1847–54.
[6] Culligan KA, Wildenschild D, Christensen BS, Gray WG, Rivers ML, Tompson AB. Interfacial area measurements for unsaturated flow through porous media. Water Resour Res 2004;40:W12413.
[7] Culligan KA, Wildenschild D, Christensen BS, Gray WG, Rivers ML. Pore-scale characteristics of multiphase flow in porous media: a comparison of air–water and oil–water experiments. Adv Water Resour 2006;29:227–38.
[8] Hassanizadeh MS, Gray WG. Mechanics and thermodynamics of multiphase flow in porous media including interphase boundaries. Adv Water Resour 1990;13(4):169–86.
[9] Hassanizadeh MS, Gray WG. Thermodynamic basis of capillary pressure in porous media. Water Resour Res 1993;29(10):3389–405.
[10] Cheng J-T, Pyrak-Nolte LJ, Nolte DD, Giordano NJ. Linking pressure and saturation through interfacial areas in porous media. Geophys Res Lett 2004;31:L08502.
[11] Berkowitz B, Hansen DP. A numerical study of the distribution of water in partially saturated porous rock. Trans Porous Media 2001;45:303–19.
[12] Gladkikh M, Bryant S. Prediction of interfacial areas during imbibition in simple porous media. Adv Water Resour 2003;26:609–22.
[13] Reeves PC, Celia MA. A functional relationship between capillary pressure, saturation and interfacial area as revealed by a pore-scale network model. Water Resour Res 1996;32(8):2345–58.
[14] Held RJ, Celia MA. Modeling support of functional relationships between capillary pressure, saturation, interfacial area and common lines. Adv Water Resour 2001;24:325–43.
[15] Dalla E, Hilpert M, Miller CT. Computation of the interfacial area for two-fluid porous systems. J Contam Hydrol 2002;56:25–48.
[16] Joekar-Niasar V, Hassanizadeh SM, Leijnse A. Insights into the relationship among capillary pressure, saturation, interfacial area and relative permeability using pore-network modeling. Transp Porous Med 2007;74(2):201–19. doi:10.1007/s11242-007-9191-7.
[17] Helland J, Skjaeveland S. Relationship between capillary pressure, saturation, and interfacial area from a model of mixed-wet triangular tubes. Water Resour Res 2007;43:W12S10. doi:10.1029/2006WR005698.
[18] Martys NS, Chen H. Simulation of multicomponent fluids in complex three-dimensional geometries by the lattice Boltzmann method. Phys Rev E 1996;53(1):743–50.
[19] Tölke J, Krafczyk M, Schulz M, Rank E. Lattice-Boltzmann simulations of binary fluid flow through porous media. Philos Trans R Soc London A 2000;360:535–45.
[20] Bekri S, Alder P. Dispersion in multiphase flow in porous media. Int J Multiphase Flow 2001;28:665–9.
[21] Sukop M, Or D. Invasion percolation of single component, multiphase fluids with lattice-Boltzmann models. Physica B 2003;338:298–303.
[22] Pan C, Hilpert M, Miller CT. Lattice-Boltzmann simulation of two-phase flow in porous media. Water Resour Res 2004;40:W01501. doi:10.1029/2003WR002120.
[23] Vogel H-J, Tölke J, Schulz V, Krafczyk M, Roth K. Comparison of a lattice-Boltzmann model, a full-morphology model, and a pore network model for determining capillary pressure–saturation relationships. Vadose Zone J 2005;4:380–8.
[24] Li H, Pan C, Miller CT. Pore-scale investigation of viscous coupling effects for two-phase flow in porous media. Phys Rev E 2005;72:026705. doi:10.1103/PhysRevE.72.026705.
[25] Schaap MG, Porter ML, Christensen BS, Wildenschild D. Comparison of pressure–saturation characteristics derived from computed tomography images and lattice-Boltzmann simulations. Water Resour Res 43. doi:10.1029/2006WR005730.
[26] Ahrenholz B, Tölke J, Lehmann P, Kaestner A, Krafczyk M, Durner W. Prediction of capillary hysteresis in a porous material using lattice-Boltzmann methods and comparison to experimental data and a morphological pore network model. Adv Water Resour 2008;31:1151–73. doi:10.1016/j.advwatres.2008.03.009.
[27] Shan X, Chen H. Lattice-Boltzmann model for simulating flows with multiphases and components. Phys Rev E 1993;47:1815–9.
[28] Shan X, Chen H. Simulations of non-ideal gases and liquid-gas phase transitions by the lattice-Boltzmann equation. Phys Rev E 1994;49:2941–8.
[29] Chen S, Doolen G. Lattice-Boltzmann method for fluid flows. Annu Rev Fluid Mech 1998;30:329–64.
[30] Sukop MC, Thorne DT. Lattice Boltzmann modeling an introduction for geoscientists and engineers. Springer; 2006.
[31] Porter ML, Wildenschild D. Image analysis algorithms for estimating porous media multiphase flow variables from computed microtomography data: a validation study, Comput Geosci. doi:10.1007/s10596-009-9130-5.
[32] McClure J, Adalsteinsson D, Pan C, Gray W, Miller C. Approximation of interfacial properties in multiphase porous media systems. Adv Water Resour 2007;30(1):354–65.
[33] McClure J, Pan C, Adalsteinsson D, Gray W, Miller C. Estimating interfacial areas resulting from lattice-Boltzmann simulation of two-fluid-phase flow in a porous medium. In: Miller CT, Farthing MW, Gray WG, Pinder GF, editors, Computational methods in water resources XV, vol. 1; 2004.
[34] Niessner J, Hassanizadeh MS. A model for two-pase flow in porous media including fluid–fluid interfacial area. Water Resour Res 2008;44:W08439. doi:10.1029/2007WR006721.
[35] Niessner J, Hassanizadeh MS. Multiphase flow research chapter 12: two-phase flow and transport in porous media including fluid–fluid interfacial area. Nova Sci 2009;1–20.